INSTRUMENTS AND METHODS OF INVESTIGATION

X-ray refraction introscopy

V V Lider

Contents

Abstract. The review describes the operating principles and capabilities of X-ray refraction introscopy, which involves the use of a crystal analyzer as an angular filter. Methods for obtaining absorption, refraction, and extinction contrast, and various image processing algorithms to implement two-dimensional and three-dimensional visualization are considered. Also given are examples of applying the method in biomedicine and materials science.

Keywords: X-rays, refraction, diffraction, small-angle scattering, introscopy, crystal analyzers, visualization

1. Introduction

Imaging the internal macrostructure of an object in X-ray radiation is an important diagnostic tool in medicine, biology, and materials science. It was no coincidence that X-rays with high penetrating power were chosen for this purpose. With their help, the structure of the interior of an object can be examined without destroying it.

The refractive index in the X-ray region is represented as $n = 1 - \delta + \mathrm{i}\beta$, where δ is the decrement of the X-ray refractive index, and β is the coefficient describing the attenuation of intensity due to X-ray absorption by the substance. Parameters δ and β are described by the formulas [1]

$$\delta = \frac{\rho \lambda^2 r_0 \, N_{\mathrm{A}} Z}{2\pi A} \, , \qquad (1)$$

$$\beta = \frac{\mu \lambda}{4\pi} \, , \qquad (2)$$

V V Lider. Kurchatov Crystallography and Photonics Complex,
Leninskii prosp. 59, 119333 Moscow, Russian Federation
E-mail: vallider@yandex.ru

where λ is the radiation wavelength, N_{A} is Avogadro's number, r_0 is the classical radius of the electron, ρ is the density of the substance, Z and A are the atomic number and atomic weight of the sample material, respectively, and μ is the linear absorption coefficient.

X-ray absorption radiography long ago established itself as a unique research technique. However, for a number of applications, especially when imaging low-absorbing objects such as biological tissues, traditional absorption radiography cannot be used effectively, because the X-ray absorption in such objects is extremely low. An estimate of the δ and β values for biological tissues has shown that $\delta = 10^{-6} - 10^{-8}$, approximately 10^3 times greater than $\beta \, (10^{-9} - 10^{-11})$ for X-rays in the energy range of 10–150 keV. Therefore, the differences in the X-ray phase shift for tissues with different densities are much greater than those in linear absorption coefficients. Consequently, phase contrast imaging can significantly improve the sensitivity of X-rays to small changes in the structure of the objects under study.

Furthermore, the absorption contrast falls off rapidly at high energies E, being proportional to E^{-4}, while the refractive contrast is proportional to E^{-2}. Therefore, visualization can be performed at higher energies without noticeable loss of contrast with a significant reduction in the radiation dose delivered to tissues [2], which is very important when conducting *in vivo* biomedical research. For example, in mammographic studies, Pisano and his colleagues found that the radiation dose decreased by 15 times when the X-ray energy was increased from 18 to 30 keV [3].

The method is very effective for studying weakly absorbing objects with small variations in the absorption coefficient within the object: important for the method are variations in the decrement of the refractive index δ in the object under study. The lateral gradient δ is responsible for the deviation in X-rays. When the normal to the interface where the object density changes from ρ_1 to ρ_2 makes an angle α with the incident ray, the ray is deflected by $\gamma = (\delta_1 - \delta_2)\tan\alpha = \Delta\delta \tan\alpha$. Refractive effects are strongest when α is close to $90°$, i.e., at the lateral boundaries of the object. If the direction

of propagation is z and the direction of deflection is y, then $\tan \alpha = \mathrm{d}z/\mathrm{d}y$ and $\gamma = (\lambda/2\pi)(\mathrm{d}\varphi/\mathrm{d}y)$.

An X-ray phase contrast image was first obtained using a crystal monoblock interferometer [4], in which, as a result of the interference of the reference beam with the beam passing through the sample under study, a standing wave is formed, which is analyzed by the crystal lattice of the analyzer. The second method for obtaining a phase-contrast image uses the so-called Talbot interferometer, which consists of two diffraction gratings that act as a modulator and a phase front analyzer [5]. The propagation-based imaging method was proposed by Snigirev et al. [6]. This method uses Fresnel diffraction to increase the visibility of the edges and boundaries of the object under study.

This review is devoted to a method which allows an unusually strong increase in the contrast of weakly absorbing materials due to a combination of the effects of refraction and scattering of X-rays. In the English-language literature, it is called Analyzer-Based Imaging (ABI) or Diffraction Enhanced X-Ray Imaging (DEI). In the Russian-language scientific literature, this method is often referred to as "X-ray Refractive Introscopy" (for example, Refs [7–9]).

X-ray refractive introscopy (XRI) was first proposed by Forster et al. [10]. The last decade of the twentieth century was marked by increased interest of researchers in this method [7, 11–21], and it has become widespread in biomedicine [22, 23] and materials science [24].

2. Two-dimensional (2D) X-ray refraction introscopy

Figure 1 shows an optical diagram of an experimental setup using synchrotron radiation (SR). The use of SR as a source of X-ray radiation has paved the way for XRI to become one of the main methods of biomedical imaging.

In order to transfer technologies developed using SR sources to the clinic, compact laboratory X-ray sources are needed. In the case of XRI, encouraging results were obtained using standard sources [12, 16, 26–29].

In the XRI method, the sample under study is placed between the crystals of a double-crystal diffractometer [23, 30, 31] (see Fig. 1). Its first monochromator crystal limits the angular and spectral divergence of the primary X-ray beam. The second analyzer crystal, located between the sample and the detector, plays the role of an angular filter, which cuts out only a narrow angular interval from the beam passing through the sample. This interval is determined by the width of the rocking curve at its half-maximum (the width of the rocking curve), whose value can be determined by changes in the intensity of the diffracted X-rays during angular scanning of the analyzer crystal in the vicinity of the Bragg angle.

The setup for refractive contrast formation for XRI is shown in Fig. 2. Object of study *1* is placed in a quasi-plane wave produced by the preliminary reflection of X-ray radiation from a monochromator crystal. Located behind the object in the Bragg geometry is crystal analyzer *2*. The image is recorded in the reflected beam with pixel detector *3*. When the analyzer is mounted in an angular position on the slope of the rocking curve, intensity modulation can be carried out owing to the deflection of X-rays due to refraction. At this point in the rocking curve, the intensity modulation changes approximately linearly with the refractive angle. To state it in different terms, the change in refractive angle or change in phase (i.e., the first derivative
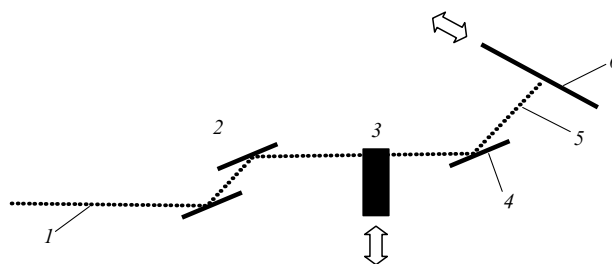
Figure 1. Experimental XRI setup at the SR station. *1* — ribbon-shaped SR beam, *2* — double-crystal monochromator, *3* — sample, *4* — analyzer crystal, *5* — diffracted X-ray beam, *6* — detector. Arrows indicate the direction of simultaneous scanning of the sample and detector [25].
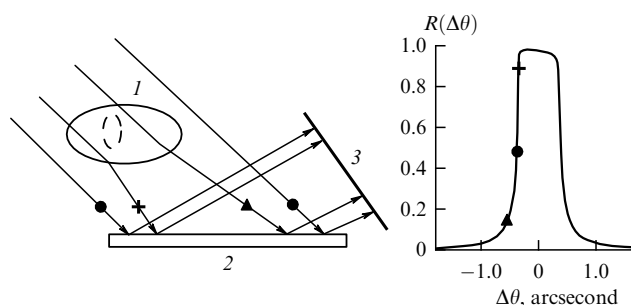
Figure 2. Experimental setup for recording phase-contrast images. *1* — sample, *2* — analyzer crystal, *3* — detector; $R(\Delta\theta)$ is the rocking curve of the symmetric (422) diffraction reflection of AgKα radiation by a silicon single crystal [20].

of the X-ray phase) is directly reflected by the change in intensity due to this linear relationship. The strongest image contrast dynamics are achievable under precisely these conditions.

The phase gradients inherent in the sample locally deflect the X-rays from the direction of initial propagation. The run of the three X-rays is indicated by •, +, and ▲. The ray (•) is incident on the analyzer without refraction in the sample. In practice, this is possible, for example, in the absence of a sample or in the passage through the center of a cylindrical object. The ray (▲), having undergone refraction in the sample, is incident on the analyzer at a smaller angle compared to the unrefracted ray, and the ray (+) is refracted in the other direction, so it is incident on the analyzer at a larger angle. If the initial operating point (OP) is located on the low-angle slope of the analyzer's rocking curve (recall that in double-crystal diffractometry the operating point describes the angular position of the second crystal relative to the first one), then a change in the direction of the beam (▲) corresponds to a movement of the OP towards smaller angles, and a change in the direction beam (+) towards larger angles. This will lead, respectively, to a decrease and increase in the intensity recorded by individual pixels of the detector (see Fig. 2). It is clear that, when the OP is positioned on the opposite slope of the rocking curve, while the result will be the opposite: the ray (▲) will cause an increase in intensity, while the ray (+) will cause its decrease [32]. As a result, even small changes in the angles of incidence of X-rays on the analyzer lead to a significant change in the intensity of the diffraction reflection.

It should be noted, however, that the analyzer 'sees' only that component of the sample density gradient which is

parallel to the diffraction plane, so that the refractive contrast tends to zero in the plane normal to the diffraction plane, which is a disadvantage of the XRI method.

For radiation with wavelength $\lambda \sim 1$ Å, the angles of refraction γ are units and fractions of arcseconds. However, such small deviations can lead to very significant image contrast. This is due to the fact that the angular width of the rocking curves is comparable to the value of δ.

An important issue is the limiting sensitivity of the method to changes in the refractive index. From the theory developed in Ref. [17], it follows that it is possible to record a change in the refractive index decrement $\Delta\delta \sim 10^{-9}$, which is three orders of magnitude lower than the refractive index decrement $\delta \sim 10^{-6}$ for soft tissues of most biomedical objects.

It is clear from Fig. 2 that the slope of the rocking curve acts as a contrast enhancer: the steeper the slope, the greater the change in image intensity to be expected due to the effects of X-ray refraction.

To a first approximation, the steepness of the slope of the rocking curve is determined by its experimental width $\omega_{\exp}$ [33]:

$$\omega_{\exp}^2 = \omega_0^2 + \omega_{\mathrm{dev}}^2 = \omega_0^2 + \omega_{\mathrm{M}}^2 + \left(\frac{\delta\lambda}{\lambda}\right)^2 (\tan\theta_{\mathrm{M}} - \tan\theta_0)^2 . \tag{3}$$

Here, ω_{dev} is the instrumental function, ω_{M} and $\delta\lambda/\lambda$ are the angular and spectral widths of the X-ray beam produced by the monochromator, ω_0 is the width of the sample's own rocking curve, and θ_{M} and θ_0 are the Bragg angles for the reflections of the monochromator and analyzer.

As follows from formula (3), to obtain the intrinsic rocking curve, the instrumental function has to be reduced, i.e., it is desirable to fulfill the conditions

$$\omega_{\mathrm{M}}^2 \ll \omega_0^2 , \tag{4}$$

$$\left(\frac{\delta\lambda}{\lambda}\right)^2 (\tan\theta_{\mathrm{M}} - \tan\theta_0)^2 \ll \omega_0^2 . \tag{5}$$

The first inequality is easy to satisfy by using an asymmetrically cut monochromator crystal, when [34, 35]

$$\omega_{\mathrm{M}} = \omega_{\mathrm{i}} b = \omega_{\mathrm{s}} b^{1/2} , \tag{6}$$

where ω_{M} is the angular divergence of the beam at the output of the monochromator; ω_{i} is the acceptance angle of the monochromator (the rocking curve at the monochromator input); b is its asymmetry factor:

$$b = \frac{\sin(\theta - \phi)}{\sin(\theta + \phi)} , \tag{7}$$

with ϕ being the angle between the system of reflecting planes and the crystal surface; and ω_{s} is the width of the rocking curve for the symmetric reflection ($b = 1$) of the monochromator:

$$\omega_{\mathrm{s}} = \frac{2C|\chi_{\mathrm{hr}}|}{\sin(2\theta_{\mathrm{B}})} , \tag{8}$$

$$\chi_{\mathrm{hr}} = -\left(\frac{r_0\lambda^2}{\pi V}\right)F_{\mathrm{hr}} ,$$
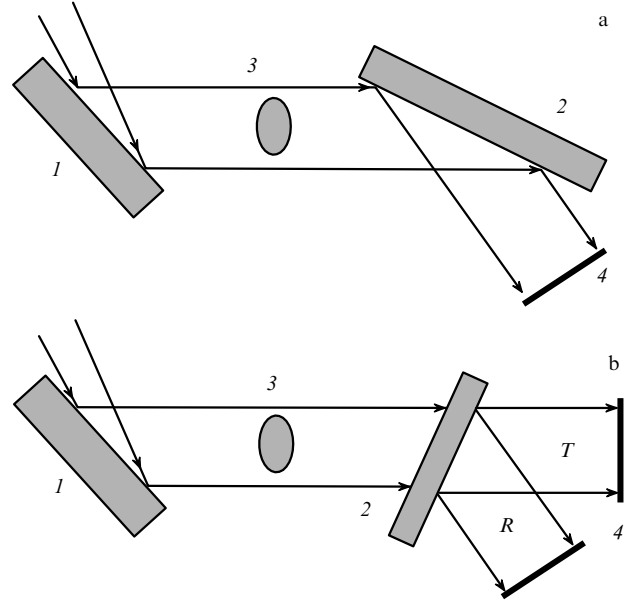
Figure 3. Optical configuration of parallel nondispersive XRI using an asymmetric monochromator and an analyzer crystal in the Bragg (a) and Laue (b) geometries: *1* — monochromator, *2* — analyzer, *3* — object of study, *4* — detectors; *T* and *R* are the transmitted and diffracted beams, respectively.

where θ_{B} is the Bragg angle, χ_{hr} is the real part of the Fourier component of the crystal polarizability, the polarization factor $C = 1$ for wave field components polarized perpendicular to the diffraction plane (σ-polarization) and $C = \cos(2\theta_{\mathrm{B}})$ for components polarized in this plane (π-polarization), V is the volume of the unit cell, r_0 is the classical electron radius, and F_{hr} is the real part of the structural amplitude.

So, an asymmetrically cut crystal monochromator for ω_{M} is capable of reducing the angular divergence ω_{M} of the X-ray beam.

As a rule, symmetrical reflections of the analyzer are used in XRI. The authors of Ref. [36] made an attempt to reduce the width of its rocking curve by using an asymmetric reflection during transmission diffraction (in the Laue geometry). Other ways to increase the steepness of the slopes of the rocking curve of the analyzer crystal involve the use of harder X-ray radiation or higher-order reflections [37].

We now revert to inequality (5), which is the mathematical representation of the condition for dispersion-free (or quasi-dispersion-free) X-ray diffraction. Clearly, to satisfy condition (5), it is enough to direct one of the factors on its left side to zero, for example, to select the reflections of the monochromator and the crystal under study in such a way that the corresponding interplanar distances (and, consequently, the Bragg angles of θ_{M} and θ_0) are close in magnitude and the reflecting planes are parallel.

In this case, it is customary to talk about a parallel dispersion-free diffraction scheme, and the analyzer crystal can be in the Bragg or Laue geometry (Fig. 3).

As is clear from geometric considerations, when using an asymmetric reflection of a monochromator in the Bragg geometry, the beam dimensions in the diffraction plane at the input S_0 and output S_{h} of the crystal are related by the relation

$$S_{\mathrm{h}} = \frac{S_0}{b} . \tag{9}$$

Thus, the use of an asymmetrically cut monochromator makes it possible to increase the front of the X-ray beam and, therefore, to obtain images of large samples in an enlarged field of view without the need to scan the sample (see Fig. 3).

The spatial resolution of XRI is mainly determined by the pixel size of the X-ray detector: when use is made of an asymmetric monochromator, the effective distance [38] between the X-ray source and the sample can be made much longer than the sample–detector distance.

High-resolution XRI can be implemented by converting X-ray radiation into visible light with scintillation crystals and then focusing the light onto a CCD camera via an optical lens [39]. For example, the pco.1600 camera (1600 × 1200 pixels) combined with a lens system and a 50-μm-thick CdWO$_4$ (CWO) scintillation screen provided an effective pixel size of 4×4 μm, capturing a field of view of about 6.3×4.7 mm [40, 41].

The result of wave field propagation during Laue diffraction in the Bormann triangle formed by two plane X-ray waves (one along the direction of the incident beam, the other along the direction of the diffracted beam) is image blurring. Therefore, the Laue analyzer degrades the image quality. It is possible to reduce the degradation of spatial resolution by reducing the base of the triangle, i.e., due to the thinning of the analyzer. It is also possible to reduce the size of the base of the Bormann triangle by reducing the angle $2\theta_B$ at the apex of the triangle. This calls for a shorter X-ray wavelength or a choice of reflections with high Miller indices [42].

2.1 Refraction visualization

The contrast of the resultant XRI images depends on the position of the OP on the rocking curve of the analyzer crystal (Fig. 4). Absorption contrast arises from differences in the density and thickness between adjacent regions of the sample and is visualized when the OP is positioned at its apex; refractive contrast emerges at the boundary between these regions, and it is highest when the OP is positioned on the slope of the rocking curve, but is observed against the background of absorption contrast. One option for getting rid of the contribution of absorption contrast is to obtain an image in a dark field, for example, when moving the OP to the tail of the rocking curve (Fig. 4c).

In X-ray topography, this technique is referred to as the 'weak beam method' and is used to visualize small deformation fields produced by structural defects in crystals [44, 45]. However, the method requires long exposures, which limits its application, for example, in biomedicine.

Another dark-field X-ray imaging system uses an asymmetric monochromator and a symmetric analyzer in the Laue geometry (Fig. 3b) [46, 47].

The propagation of two types of Bloch standing waves in a crystal with close phase velocities gives rise in the total self-consistent wave field to spatial depth beats over a distance Λ, called the extinction length [48, 49].

The existence of such beats gives rise to a potential energy transfer from a transmitted wave to a diffracted wave and back. However, it should be remembered that the self-consistent wave field exists inside the crystal, and real transfer is observed only at the output surface of the crystal. For the symmetric Laue case of X-ray diffraction by a transparent plane-parallel crystalline plate of thickness t (the reflecting planes are perpendicular to the surface), when the
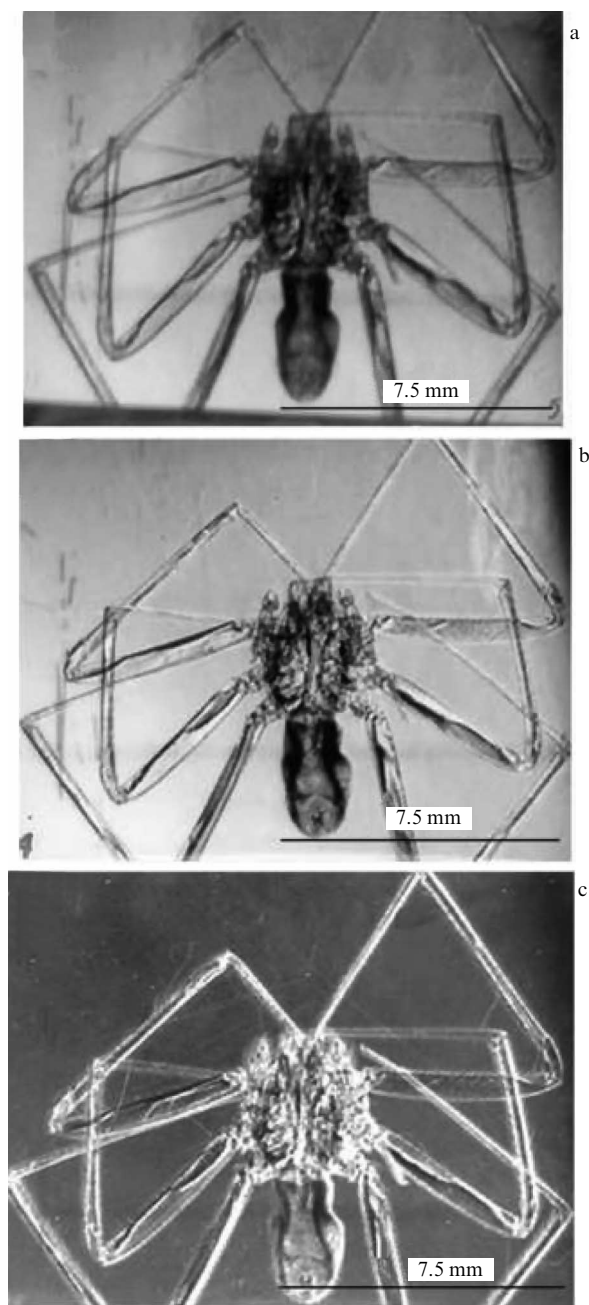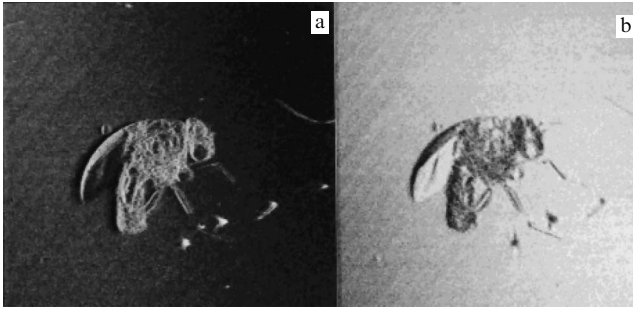

Figure 4. Images of a gaucho spider (*Loxosceles gaucho*) obtained at different angular positions of OP on the rocking curve of the analyzer in Bragg geometry: at the top (a), on the slope (b), in the tail (c). Bragg asymmetric (monochromator) and symmetric (analyzer) based on monocrystalline silicon, reflection (333), $E = 8$ keV, $\omega_0 \sim 10$ μrad [43].

diffraction conditions are strictly satisfied, the intensities of the diffracted R and transmitted T waves are given by the expressions

$$R = \sin^2\left(\frac{\pi t}{\Lambda}\right), \tag{10}$$

$$T = \cos^2\left(\frac{\pi t}{\Lambda}\right), \tag{11}$$

$$\Lambda = \frac{\lambda \cos\theta}{C|\chi_{hr}|}. \tag{12}$$

Figure 5. Dark- (a) and bright-field (b) images of an insect (field size: 5×5 mm) obtained using an analyzer crystal in Laue geometry [47].

Expression (10) shows that the intensity R at points with coordinates $t/\Lambda = m$ periodically vanishes, and at points $t/\Lambda = m + 1/2$ it has a maximum value $R = 1$. The $T(t)$ dependence is in antiphase with the $R(t)$ dependence.

In general, at any depth t, the law of energy conservation is satisfied: $R + T = 1$ [50].

By selecting the energy of the primary beam and the thickness of the analyzer crystal, it is possible to achieve the following conditions: $R = 1$, $T = 0$, when the intensity of the transmitted beam is practically equal to zero. This means that the transmitted beam consists only of X-rays that changed their trajectory as a result of interaction with the sample. In this case, due to the weak (zero) background, one can expect to obtain high-contrast images (Fig. 5a).

In Ref. [51], a very high transmittance was obtained for X-rays refracted by the sample and complete suppression of the transmitted direct beam, which was provided by a single-crystal silicon platelet 1.075 mm in thickness (reflex (440), $E = 35$ keV). Images of biomedical samples obtained in this way showed exceptionally high contrast with a spatial resolution of no worse than 5 μm. The authors of Ref. [52] reduced the thickness of the analyzer crystal to 150 μm (reflection (440), $E = 31$ keV). This provided a spatial resolution of 1.3 μm in the diffraction plane.

This method has found application in medicine for imaging bone tissue [53], articular cartilage [54, 55], and breast samples [56].

2.2 Absorption and refraction visualization

The dark-field X-ray imaging methods discussed above are based on the suppression of refractive contrast, which deprives the researcher of additional information about the structural features of the object under study.

Several algorithms have been proposed to separate absorbtion and refraction signals. The earliest formalism was an approach based on the geometric optics approximation [57], which used two images obtained on each slope of the rocking curve [19]. The algorithm (hereinafter referred to as Chapman's algorithm) used a linear approximation of the slopes of the rocking curve obtained without a sample. The basic hypothesis underlying the algorithm is that refractive angles are small compared to the width of the rocking curve, so that the rocking curve can be described reasonably well by the first-order Taylor approximation.

Chapman et al. [19] came up with the idea to generate refractive $\Delta\theta$ and I_R absorption images by solving the system

$$I_L = I_R R(\theta_L + \Delta\theta) = I_R \left[R(\theta_L) + \left(\frac{dR}{d\theta} \right)(\theta_L)\Delta\theta \right], \quad (13)$$
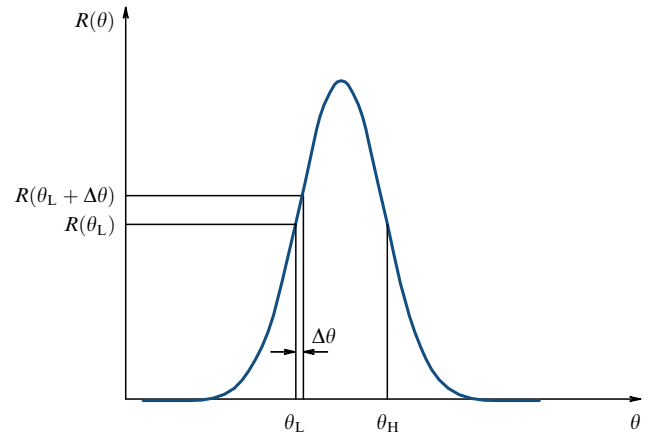
Figure 6. Experimental rocking curve shows OP position corresponding to angle θ_L. Intensities I_L and I_H are measured on slopes corresponding to smaller and larger angles θ_L and θ_H [58] (see body of text and formulas (13), (14)).

$$I_H = I_R R(\theta_H + \Delta\theta) = I_R \left[R(\theta_H) + \left(\frac{dR}{d\theta} \right)(\theta_H)\Delta\theta \right], \quad (14)$$

where I_L and I_H denote the intensity of the images on the low-angle slope (θ_L) and on the higher-angle side (θ_H) of the rocking curve, I_R is the intensity of the X-ray beam attenuated by absorption in the sample, $R(\theta)$ is the height of the rocking curve for OP in position θ, and $\Delta\theta$ is the angle of refraction in the diffraction plane by which the X-rays deviate from the initial direction when passing through the sample (Fig. 6).

As a result, we obtain

$$I_R = \frac{I_L(dR/d\theta)(\theta_H) - I_H(dR/d\theta)(\theta_L)}{R(\theta_L)(dR/d\theta)(\theta_H) - R(\theta_H)(dR/d\theta)(\theta_L)}, \quad (15)$$

$$\Delta\theta = \frac{I_H R(\theta_L) - I_L R(\theta_H)}{I_L(dR/d\theta)(\theta_H) - I_H(dR/d\theta)(\theta_L)}. \quad (16)$$

The phase shift can be determined from Eqn (16) on a pixel-by-pixel basis [59].

The rocking curve can be satisfactorily linearized only when the object does not introduce large phase gradients into the incident wave field [60], which limits the applicability of the approach under consideration.

If measurements are taken at symmetrical points on the slopes of the rocking curve, then $(dR/d\theta)(\theta_H) = -(dR/d\theta)(\theta_L)$. If pairs of data are taken for measurements at $\theta_H = \omega_{exp}/2$ and $\theta_L = -\omega_{exp}/2$, then $R(\theta_L) = R(\theta_H) = R_p/2$, where R_p is the peak reflectivity of the analyzer. Under these conditions, equation (16) reduces to the formula [37]

$$\Delta\theta = -\left[\frac{R_p}{2(dR/d\theta)_{(-\omega/2)}} \right] \frac{(I_H - I_L)}{(I_H + I_L)}. \quad (17)$$

When using an analyzer in the Laue geometry, the transmitted and diffracted beams contain mutually complementary contrast information, and the use of two detectors allows one to obtain both absorption and phase images in one exposure, which reduces measurement time and radiation dose [52, 61–64]. Then, to obtain absorption $\rho t(y, z)$ and refraction angle $\Delta\theta(y, z)$ maps, one can use formulas (18),

(19), which are similar to formulas (15), (16) [61]:

$$\rho t(y, z)$$

$$= -\left(\frac{\rho}{\mu}\right) \ln \left\{ \frac{I_T(y,z)(\partial R/\partial \theta)(\theta_0) - I_D(y,z)(\partial T/\partial \theta)(\theta_0)}{I_0 \left[T_0(y,z)(\partial R/\partial \theta)(\theta_0) - R_0(y,z)(\partial T/\partial \theta)(\theta_0) \right]} \right\},$$
$$(18)$$

$$\Delta \theta(y, z) = \frac{I_D(y,z) T(\theta_0) - I_T R(\theta_0)}{I_T(y,z)(\partial R/\partial \theta)(\theta_0) - I_D(y,z)(\partial T/\partial \theta)(\theta_0)}, \quad (19)$$

where I_0, I_D, and I_T represent the intensities of the primary, diffracted, and transmitted beams, respectively, at the detector pixel with coordinates y, z; $R_0(\theta_0)$ and $T_0(\theta_0)$ are the heights of the rocking curve of the diffracted and transmitted beams, respectively, with the OP in position θ_0 on the rocking curve in the absence of a sample, and $R(\theta_0)$ and $T(\theta_0)$ are those with a sample.

The algorithms outlined above provide an elegantly simple reconstruction using a first-order Taylor series approximation of the rocking curve, which essentially models the rocking curve as a triangular function. This approximation masks subtle features of the real rocking curve, limits the range of refractive angles that can be measured, and can lead to significant image errors.

The admissible range of refractive angles was expanded by including nonlinear terms of the rocking curve [65], improving the fit of the rocking curve using a polynomial curve [66] and a Gaussian function. Fitting the rocking curve with a Gaussian function was found to provide the best approximation of a bell-shaped rocking curve [67]. However, the Gaussian function may fail to accurately model the peak and tails of the rocking curve [67]. Hall et al. [68] showed that the Type-VII Pearson distribution,

$$y = c \left[1 + \frac{(x - x')^2}{ma^2} \right]^{-m}, \quad (20)$$

can be effectively used for fitting X-ray diffraction peaks. Here, c defines the amplitude, x' is the center of gravity, and a and m determine the distribution profile. Parameters a, c, and $m > 0$ and $-\infty < x < \infty$. This function has the limits of the Cauchy distribution ($m = 1$), modified Lorentz distribution ($m = 2$), and Gaussian distribution ($m \to \infty$). The usefulness of this function stems from its small number of parameters and ability to converge to several types of bell-shaped functions.

Due to the multitude of functions that the Type VII Pearson distribution covers, it can provide a better fit to symmetric rocking curves than the Gaussian, Lorentz, or Cauchy distributions. Substituting the reflection coefficient $R(\theta + \Delta\theta)$ into Eqns (13) and (14), the recorded intensity can be approximated by the expression

$$I_{L,H} = c I_R \left[1 + \frac{(\theta_{L,H} + \Delta\theta)^2}{ma^2} \right]^{-m} \quad (21)$$

for $x' = 0$. Here, θ_L and θ_H can be any two orientations of the analyzer crystal that are not limited by the points of half-maximum reflectivity. Dividing I_L by I_H, one can find the angle of refraction:

$$\Delta\theta = \frac{\theta_H - B\theta_L \pm \left[B(\theta_H - \theta_L)^2 - ma^2(B-1)^2 \right]^{1/2}}{B - 1}, \quad (22)$$

where $B = (I_L/I_H)^{1/m}$. Then, the contribution of X-ray absorption to the sample image can be determined:

$$I_R = \left(\frac{I_{L,H}}{c} \right) \left[1 + \frac{(\theta_{L,H} + \Delta\theta)^2}{ma^2} \right]^m. \quad (23)$$

This provides a straightforward solution for phase recovery on a pixel-by-pixel basis [69].

In the geometric optics approximation, the Type-VII Pearson distribution provides a more accurate method for recovering amplitude and phase information than an approach based on the linear approximation of the rocking curve.

In the case of a Laue analyzer, one can separate the diffracted I_D and transmitted I_T intensities and fit the Type-VII Pearson function to the resultant rocking curve [70, 71]:

$$\frac{I_D}{I_T} = \frac{I_R R(\theta)}{I_R T(\theta)} = c \left(1 + \frac{\theta^2}{ma^2} \right)^{-m}. \quad (24)$$

The center of gravity of this curve was defined here as zero. Transformation of Eqn (24) allows finding the angle of incidence of the ray on the crystal:

$$\theta = \pm a \left\{ m \left[\left(\frac{I_T}{I_D} \right)^{1/m} - 1 \right] \right\}^{1/2}. \quad (25)$$

Equation (25) gives θ_0 in the absence of a sample and θ_s with a sample. The angular X-ray deviation by the sample can be found using the equation $\Delta\theta = \theta_s - \theta_0$. After introducing (to avoid confusion) new parameters, the transmission rocking curve is approximated by the inverted Type-VII Pearson function:

$$I_T = I_R T(\theta) = I_R \left[f - d \left(1 + \frac{\theta^2}{nb^2} \right)^{-n} \right]. \quad (26)$$

The absorption image is found by transforming Eqn (26):

$$I_R = I_T \left[f - d \left(1 + \frac{\theta^2}{nb^2} \right)^{-n} \right]^{-1}. \quad (27)$$

2.3 Extinction visualization

In addition to absorption and refraction, small-angle scattering (SAS) of X-rays also plays an important role in producing image contrast [22]. In the general case, we can assume that SAS arises from inhomogeneities whose size is smaller than the spatial resolution of the detector. Multiple scattering from such inhomogeneities does not entail a displacement of the beam passing through the inhomogeneity region but gives rise to its angular broadening.

The result of SAS is a noticeable change in the shape of the rocking curve: the peak value of the rocking curve becomes lower (the so-called extinction effect) and the signal at its tails increases [72, 73].

Since the algorithms discussed above ignore the SAS, their application is evidently limited to the study of objects that do not contain microinhomogeneities. However, micrometer-sized particle systems are found in many biological and nonbiological porous materials, for example, microvoids and pores [74], suspensions of microspheres and microbubbles [75, 76], microcracks [77], pulmonary alveoli [78], and collagen, which is a fibrous protein that is the main component of the connective tissue of the mammary gland [79].

Objects that produce mainly SAS will produce a weak signal or no signal at all on the slope of the rocking curve, and therefore the algorithm described in Ref. [19] is not applicable. Given these limitations, Rigon et al. focused on samples producing only absorption and SAS, i.e., on the case where the refraction is negligible, and introduced a modified two-image algorithm [80]. Although formally similar to the original formulation developed by Chapman et al. [19], this approach considers a second-order Taylor expansion and combines two images obtained at the peak and tail of the rocking curve, where the second derivative is greatest. Then, in some approximations, two equations are obtained and solved, giving the image of absorption and SAS [80].

To visualize the SAS produced by defects arising from various treatments of composite materials and steels, the authors of Refs [41, 74, 81, 82] used the peak intensity of the rocking curve and the integral intensity of the X-rays recorded by the detector in the absence and presence of the object under study.

2.4 Absorption, refraction, and extinction visualization

Since a sample can generally exhibit a combination of absorption, refraction, and extinction (SAS) effects, several algorithms have been proposed to separate these physical effects and accurately quantify them [22, 83].

For a multi-parameter representation of images, these algorithms can conventionally be classed into three types according to their approaches. The first approach, the generalized Chapman algorithm, uses series of leading Taylor terms at the operating points of the rocking curve to describe intensity changes. The second one is called statistical. In it, rocking curves are parameterized from several measurements at different operating points, virtually without adjustment. The third approach involves fitting a functional form to the measured rocking curves.

2.4.1 Generalized Chapman algorithm.
Due to the limited information contained in the two images and the similarity of extinction and absorption, there was no way to determine these two properties of the object independently of each other.

Including SAS requires the introduction of higher order terms in the Taylor expansion and at least three OPs. References [73, 84] describe a generalized three-image Chapman algorithm that provides a simple way to represent the three effects in three different parametric images.

In what follows, spatial variables (x, y) will be omitted for clarity, and R_j, R_j', and R_j'' will correspond to the values of the rocking curve and its first and second derivatives calculated at the common angular position θ_j. Let $\theta_j\{j \in [1, 3]\}$ be three different positions of the OP on the rocking curve, giving

three different images $I_j = I(\theta_j)$ of the same object. A system of three equations can be obtained by writing an equation for each image I_j:

$$I_j = \left(\frac{I_R}{2}\right)\left[2R_j + 2R_j'\Delta\theta_R + R_j''(\Delta\theta_R)^2 + R_j''\sigma_{\Delta\theta}^2\right],$$

$$j \in [1, 3]. \tag{28}$$

Solving system of Eqns (28) gives three parametric images, namely the absorption image $I_R(x, y)$, the refraction image $\Delta\theta_R(x, y)$, and the SAS image $\sigma_{\Delta\theta}^2(x, y)$ (Fig. 7).

If two images (for example, I_1 and I_3) are obtained from each slope of the rocking curve, where $R_1'' = R_3'' = 0$, then solving system (28) will give the following equations:

$$I_R = \frac{I_3 R_1' - I_1 R_3'}{R_3 R_1' - R_1 R_3'}, \tag{29}$$

$$\Delta\theta_R = \frac{I_1 R_3 - I_3 R_1}{I_3 R_1' - I_1 R_3'}, \tag{30}$$

$$\sigma_{\Delta\theta}^2 = \frac{2\left[I_2/I_R - R_2 - R_2'(\Delta\theta_R)\right]}{R_2''} - \Delta\theta_R^2. \tag{31}$$

It is noteworthy that Eqns (29) and (30) are the usual equations of the Chapman algorithm (Eqns (15) and (16)). This means that, in principle, the usual Chapman algorithm also operates in the presence of SAS and can easily be integrated with the third image (I_2), which can provide information about the SAS via Eqn (31). Furthermore, if I_2 corresponds to the position of the OP at the peak of the rocking curve ($R_2' = 0$), then Eqn (31) simplifies even further:

$$\sigma_{\Delta\theta}^2 = \frac{2(I_2/I_R - R_2)}{R_2''} - \Delta\theta_R^2. \tag{32}$$

In fact, Chapman's algorithm and the algorithm proposed in Ref. [80] can be considered special cases of the general model, which are applicable when refraction or SAS is dominant.

It should be noted that the method provides quantitative information in the angular range of validity of the Taylor expansion, i.e., for small angles of refraction and scattering, on the order of several microradians, which are significantly less than the width of the rocking curve. If the scattering angle exceeds this limit, the algorithms tend to fail and saturation occurs [74]. To overcome these limitations, a new analytical algorithm [78] based on three images, called Gaussian Generalized Diffraction Enhanced Imaging (G2DEI), has been proposed, which is capable of employing a broader
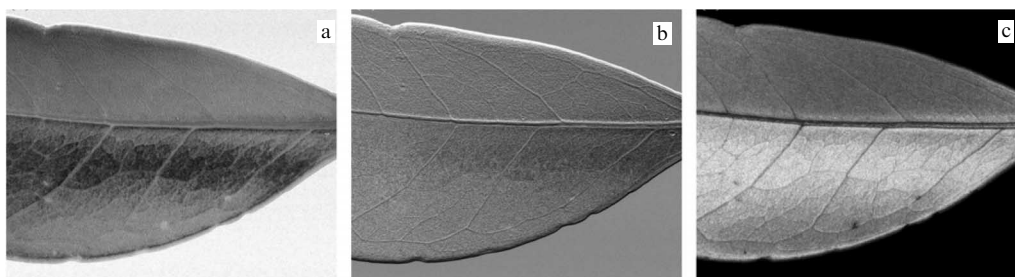
Figure 7. Parametric leaf images: (a) $I_R(x, y)$ (absorption), (b) $\Delta\theta_R(x, y)$ (refraction), (c) $\sigma_{\Delta\theta}^2(x, y)$ (SAS) [73].

range of refractive and scattering angles (more than ten μrad) that need to be provided, e.g., when studying biological objects. With this method, the experimental transmittance function of the analyzer crystal $R(\theta')$ as a function of the diffraction angle θ' can be approximated with reasonable accuracy by a Gaussian function with the standard deviation σ centered around its Bragg angle θ_B:

$$R(\theta') = \exp\left[-\frac{(\theta' - \theta_B)^2}{2\sigma^2}\right] \Longrightarrow \exp\left(-\frac{\theta^2}{2\sigma^2}\right). \quad (33)$$

The intensity $I(\theta_i, x, y)$ reaching the detector can be written as the angular convolution of the rocking curve and the scattering function:

$$I(\theta_i) = I_R\left[\frac{\sigma^2}{\sigma_S^2 + \sigma^2}\right] \exp\left[-\frac{(\theta_i - \Delta\theta_R)^2}{2(\sigma_S^2 + \sigma^2)}\right]. \quad (34)$$

Here, the peak value of the analyzer rocking curve is taken to be equal to unity and the spatial coordinates are omitted. Equation (34) contains three unknowns, namely the absorption I_R, the refraction angle $\Delta\theta_R$, and the width σ_S of the SAS distribution. Recording at least three images $I(\theta_i) = I_i$ in three different angular positions θ_i with $i = 1, 2, 3$ allows one to find the unknown $\Delta\theta_R$, σ_S, and I_R.

2.4.2 Statistical algorithms. In 2003, Pagot et al. [85], Oltulu et al. [86], and Wernick et al. [87] independently developed similar statistical methods that can reconstruct the rocking curve on a pixel-by-pixel basis by conveniently combining multiple images corresponding to different places of the rocking curve.

The authors of Ref. [87] called the method they developed Multiple-Image Radiography (MIR), since it is based on the calculation of several parametric images of an object from several images obtained.

The method involves obtaining two series of $N\,(N \geqslant 3)$ images at different positions of the analyzer crystal with and without a sample. The 'reference' (obtained without a sample) and 'object' (obtained with a sample) rocking curves are then compared. If we assume that for each pixel the angular intensity distribution is the convolution of the angular spectrum of the object with the rocking curve generation system, then the refraction, absorption, and SAS images can be calculated, respectively, from the zeroth, first, and second moments of the reference and object rocking curves [85].

The sample absorption information can be represented as [88]

$$I_{abs} = -\ln\left[\frac{\sum_{n=1}^{N} I_s(\theta_n)}{\sum_{n=1}^{N} I_b(\theta_n)}\right], \quad (35)$$

where $I_s(\theta_n)$ and $I_b(\theta_n)$ $(n = 1, 2, \ldots, N)$ denote the image intensity at angular position θ_n on the rocking curve with and without a sample, respectively.

Refraction causes a general deflection of the X-rays, which produces an angular shift in the center of gravity of the X-ray beam compared to the position in the absence of a sample [87, 89]. Since the angular shift of the center of gravity of the beam occurs only due to refractive phenomena, the refractive image of the sample can be expressed as follows:

$$\Delta\theta = \theta_s - \theta_b = \frac{\sum_{n=1}^{N} I_s(\theta_n)\theta_n}{\sum_{n=1}^{N} I_s(\theta_n)} - \frac{\sum_{n=1}^{N} I_b(\theta_n)\theta_n}{\sum_{n=1}^{N} I_b(\theta_n)}. \quad (36)$$
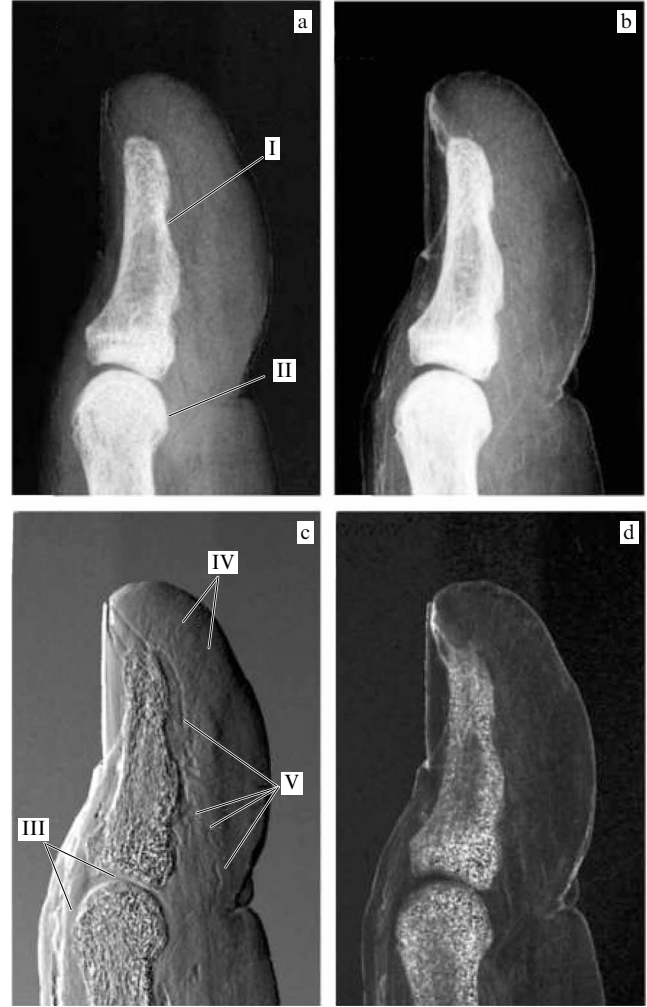
Figure 8. *In vitro* X-ray images of a human thumb measuring $2 \times 3 \times 6$ cm^3: (a) calculated absorption image, (b) absorption image, (c) refractive image, (d) extinction image. Observed anatomical structures: I and II — proximal and distal phalanges; III — tendon; IV — connective tissue; V — blood vessels [27].

The SAS image quantifies the angular divergence of the beam, and it can be defined as

$$\sigma^2 = \frac{\sum_{n=1}^{N}(\theta_n - \theta_s)^2 I_s(\theta_n)}{\sum_{n=1}^{N} I_s(\theta_n)} - \frac{\sum_{n=1}^{N}(\theta_n - \theta_b)^2 I_b(\theta_n)}{\sum_{n=1}^{N} I_b(\theta_n)}. \quad (37)$$

Images of a thumb measuring approximately $2 \times 3 \times 6$ cm^3 (Fig. 8) were acquired using 15 angular positions of the analyzer with an exposure time of 240 s at each position [27]. The thumb was moved to a horizontal position three times, since it was wider than the field of view of the X-ray beam of 12×60 mm^2.

Figure 8 shows four thumb images. The calculated absorption image shown in Fig. 8a is a representative absorption image from a conventional clinical X-ray source. The main structures, both proximal and distal phalanges, designated I and II, and the boundary between the skin of the thumb and the surrounding atmosphere are clearly visible. Tendons and other soft tissues are not visible in this case. Additional anatomical structures of the thumb are observed using other contrast mechanisms, e.g., refraction and SAS. Features such as tendons III, connective tissue IV, and blood

vessels V are found (Fig. 8b–d). Structural details are most clearly visible in the refractive image (Fig. 8c).

Statistical XRI methods were extended by Huang et al. [90, 91].

2.4.3 Fitting algorithms. However, the use of statistical methods increases visualization time and X-ray dose to the sample due to the need to obtain more images.

Another approach to extracting relevant parameters from XRI intensity distributions is to fit the functional form to the measured rocking curves with a limited number of OPs. This may be computationally intensive, but will allow flexible post-processing of the data. The Gaussian is a seemingly obvious choice for the fitting function [92], but it turns out that the Gaussian approximation cannot simultaneously correctly reproduce the rocking curve at the maximum and at the tails [24, 93].

Among various alternative rocking curve fitting functions, such as the Type-VII Pearson [94], the pseudo-Voigt function (PsdV) was found to be the most suitable to fit the experimental data. The Voigt function is the convolution of the Gaussian and Lorentz functions, while the PsdV function (Eqn (38)) is a simpler weighted sum of these two functions as a close approximation to the Voigt function:

$$I(\theta) = I_B + A \left\{ \frac{m_u (2/\pi) w}{4(\theta - \theta_c)^2 + w^2} + (1 - m_u)\left(\frac{2}{w}\right)\left(\frac{\ln 2}{\pi}\right)^{1/2} \right.$$

$$\left. \times \exp\left[\frac{-4\ln 2 (\theta - \theta_c)^2}{w^2}\right]\right\}, \tag{38}$$

where m_u is the (linear) weighting coefficient of the Lorentz and Gaussian functions.

Only three of the five different coefficients obtained from the PsdV function were useful for further evaluation, namely A, w, and θ_c. They led to different imaging modalities [24].

It was shown in [93] that a good fit invites a minimum of five OPs and that the scattering part (SAS) is characterized by Lorentzian tails, i.e., can extend to angles more than ten times the width of the rocking curve.

3. Three-dimensional (3D) X-ray refraction introscopy

Parametric XRI images are 2D images, and so the sample structures in these images often overlap and cannot show the details of the sample structure. Computed tomography (CT) can produce three-dimensional volumetric images of a sample that depict its internal structure.

Dilmanian et al. [95] in 2000 were the first to show that XRI can be used in CT mode and that XRI-CT data can be reconstructed using conventional filtered back projection (FBP) algorithms.

Compared to conventional CT, the projection data in XRI computed tomography is an integral of the partial derivative of the refractive index of the sample along the X-ray path. In XRI, the y-component of the refraction angle is recorded by an analyzer crystal, and the linear integral along the X-ray path is of the form

$$\Delta\theta(y) = \int_{-\infty}^{\infty} \left(\frac{\partial\delta(y,z)}{\partial y}\right)\mathrm{d}z, \tag{39}$$

where z is the direction of X-ray propagation, and the x-axis is perpendicular to the diffraction plane.

The gradient of the real part of the refractive index δ can be imaged using CT reconstruction from a sufficient number of projected arrays $\Delta\theta(y)$ when the object is rotated about the y-axis [95]. If the rotation occurs around the x-axis, then the integrand is $(\mathrm{d}\delta/\mathrm{d}y)\sin\varepsilon$, where ε is the angle between the X-ray and gradient directions. To reconstruct the refractive index gradient, a different algorithm is required [96].

Therefore, when the effects of absorption, refraction, and SAS are separable, three-dimensional reconstruction of the parameters of the corresponding object is possible [22, 97].

For a parallel X-ray beam, Pavlov et al. [98] proposed an indirect CT algorithm that includes second-order terms in the geometric optics approximation to describe image formation: first, it is necessary to restore the 'directional derivative projections' to the line integral of the refractive index decrement δ, and then restore δ using FBP. Maksimenko et al. [96] presented another indirect algorithm: first reconstruct $\nabla\delta$ and restore δ using integration. The authors of Ref. [99] proposed an iterative maximum-likelihood algorithm for XRI reconstruction. Compared to analytical methods, iterative reconstruction algorithms show great advantages in the presence of noise and for a small number of projections for reducing the radiation dose.

Wang et al. [100] proposed an algebraic iterative reconstruction (ART) algorithm called DEICT-ART to reconstruct the refractive index gradient of a sample. Compared with an analytical algorithm such as FBP, the ART algorithm has the advantages of noise-free reconstruction with a small number of projections. Another attractive feature of the iterative ART approach is that some types of a priori information can be incorporated into the solution. The iterative algorithm suffers from slow convergence. To speed up convergence, it is recommended to use the ordered subset algorithm [101].

Brankov et al. [89] demonstrated a CT algorithm that is a computed tomographic implementation of MIR. MIR-CT uses a set of projections obtained in the full range of the tomographic angular view of an object to reconstruct the entire volumetric image. However, in cases where the full range of angular projections cannot be obtained or when scanning time is limited, limited-angle tomography techniques may be useful. The authors of Ref. [102] studied the implementation of limited-angle CT as applied to the MIR method. To reconstruct 3D volumes from a limited number of projections, they used the Simultaneous Iterative Reconstruction Technique (SIRT) [101], which is a modification of the ART method that uses data from all projections simultaneously for each iteration and is more robust against noise than ART. The results showed that there is an optimal angular range for data acquisition, for which the method shows better performance even compared to iterative MIR-CT.

Soft tissue structures refract weakly and therefore cause only a slight bending of the X-ray wave front. As a result, an accurate phase map of soft tissue can be obtained by applying the inverse Radon transform to the resultant projection images. On the other hand, dense structures such as bones and calcifications lead to a large change in the direction of X-ray propagation. As a result, when use is made of standard methods for obtaining the inverse Radon transform, the resulting phase image has extensive artifacts near dense structures. A pre-reconstruction algorithm to overcome this

artifact near dense regions of objects was presented in Ref. [103]. To recover missing information, the algorithm iteratively processes phase and absorption images in Radon space. The disadvantage of this algorithm is that noise accumulates with each iteration step. As a result, serious microscopic artifacts appear in the resulting reconstructed image, which degrade the image with each iteration step. To reduce these artifacts, the authors of Ref. [104] presented an algorithm that includes a denoising step. The effectiveness of this algorithm was confirmed experimentally on three *in vitro* biological samples containing dense components that generate artifacts.

CT inherently requires projections in an angular range of at least 180°, which is not possible when considering the clinical application of XRI. Therefore, there is a demand for another method that will produce tomograms from a far smaller number of projection images. One possible solution to this problem is tomosynthesis [105]. The concept of tomosynthesis, which emerged in the 1930s, is the most promising technique to combine with XRI in the Laue geometry [106–109].

Standard X-ray CT using SR for imaging flat samples (such as leaves) with lateral extensions significantly larger than the detector acceptance window is rather problematic due to the strong absorption of X-rays in lateral directions. As a result, reconstructed images typically contain artifacts due to the limited available angular range. To overcome this difficulty, computed laminography with SR (CL-SR) was developed based on classical tomography and digital tomosynthesis [110, 111].

While standard CT methods are characterized by tomographic rotation around an axis perpendicular to the direction of X-ray propagation, CL-SR is characterized by a more general geometry of an inclined axis of rotation (the tomographic axis is tilted at the so-called laminographic angle $\theta < 90°$, where $\theta = 90°$ corresponds to classical CT). Given this generalized geometry, CL-SR can be applied to a broader class of objects.

In Ref. [112], the introduction of CL-SR into XRI is proposed for the observation of laterally elongated flat samples with weak absorption contrast. A generalized algorithm for obtaining multimodal 3D images of a sample is described and the basic formulas for laminographic reconstruction are presented.

4. Applications of X-ray refraction introscopy

4.1 Biomedicine

Since the mechanism of contrast formation in XRI is based not only on X-ray absorption by the object, it is ideal for simultaneous visualization of lungs, skeletal elements, cartilage, and other soft tissues [22, 23].

4.1.1 Mammography.
The enhanced soft tissue contrast of XRI is of particular importance in mammography [16]. The contrast of spicules from breast cancer lesions is significantly enhanced by both planar XRI and CT [3, 113–118].

An important circumstance regarding the prospects for the use of XRI in clinical practice was the indication that contrast enhancement is possible with a clinically acceptable radiation dose [2, 115, 119].

Due to its lesser dependence on X-ray absorption, XRI produces diagnostically useful images with a 25% reduction in breast compression [120]. For calcifications in breast tissue, XRI exhibits a fivefold higher contrast-to-noise ratio than conventional radiography [121]. Therefore, XRI can significantly improve the image quality of mammography while reducing the absorbed radiation dose and increasing patient comfort [115].

4.1.2 Osteology.
The use of XRI in joint visualization began with the fundamental work of Mollenhauer et al. [25]. More recent studies have visualized soft tissues of the foot and ankle [28, 122–127] and cartilage damage [127]. The XRI technique is one-dimensional and is sensitive only to refraction in the scattering plane. This orientation dependence of refraction can be a useful tool for understanding the internal structure of samples [128, 129]. Cooper et al. [130] used this effect to study the structure of trabecular bone in detail. Because diseases associated with bone fragility (e.g., osteoporosis) are often associated with deterioration of bone microarchitecture, studying orientation and anisotropy in bone microarchitecture may be key to predicting fractures.

In CT mode, XRI can visualize both bone and soft tissue with a high contrast [124]. The use of SR makes it possible to visualize collagen fibrils in cartilage samples with a very high spatial resolution [128, 131] and assess collagen damage in cartilage [131].

Many experiments have shown that laboratory/clinical systems will be needed to advance osteoarthritis research using XRI technology. One such study in visualizing the articular cartilage of the talus at different stages of its degeneration was reported in Ref. [29].

In cartilage studies, XRI was also used with an analyzer in the Laue geometry [55, 132].

One of the areas of application of XRI was the study of bone growth in the presence of metal implants [133–135]. Tissue engineering aims to replace or repair damaged articular cartilage with artificial tissue and as such holds great promise for joint reconstruction. Most current tissue engineering strategies combine 3D biocompatible scaffolds with viable cells and/or bioactive molecules to promote new tissue regeneration and functional restoration of cartilage. Noninvasive monitoring methods that can track the success of such scaffolds during repair processes are essential for the future development of tissue engineering strategies. The results of Ref. [136] showed that information about the scaffolds, as well as about the surrounding tissues after implantation, can be obtained using XRI-CT, which demonstrates its promise for *in vivo* studies in animals and, ultimately, for clinical studies in humans.

4.1.3 Pulmonology.
XRI demonstrates a unique contrast for the lungs [37]. The structure of the lungs is a fractal tree of respiratory tracts ending in alveoli. The specific surface area of the alveoli is large, and together with the large difference in the density of air and lung tissue, this leads to a strong SAS. The symbiosis of a Bragg monochromator and a Laue analyzer was used for *ex vivo* visualization of mouse (Fig. 9), rabbit [70, 71, 137, 138], and human lungs [139].

XRI can depict the entire extent of the lung [137] and areas of atelectasis [140] more clearly than conventional radiography.

As demonstrated in Ref. [140], in the aspiration of gastric acid, RRI was able to show the presence of fluid in the rat's lungs as a result of changes in lung density and thus

Figure 9. Reconstructed images of the thorax of a healthy mouse showing absorption (a), refraction (b), and scattering (c) information in a healthy mouse [138].
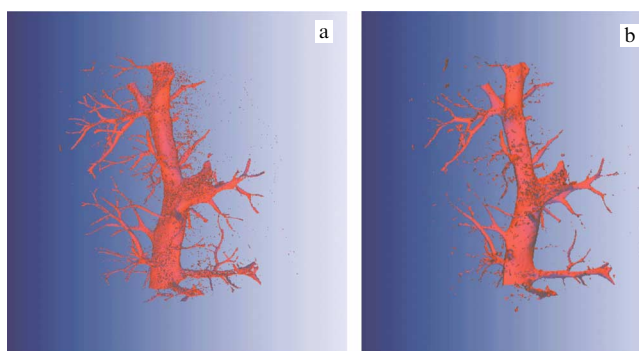
Figure 10. Two profiles of 3D reconstruction of rat liver blood vessels [88].

distinguish between healthy and damaged lung tissue more clearly than radiography.

4.1.4 Hepatology. Zhang et al. [141] showed a pronounced phase contrast in the liver vasculature of a healthy mice, which decreases with increasing liver fibrosis. Duan et al. [142] extended this analysis by showing that XRI-CT can evaluate morphological changes in the hepatic microvasculature resulting from fibrosis. Hu et al. [143] showed a 1.4-fold and 2-fold reduction in vascular density in fibrotic and cirrhotic rats, respectively.

Three-dimensional images of rat liver blood vessels are shown in Fig. 10. They clearly display the vascular branching structure and morphology of the blood vascular tree with a minimum blood vessel diameter of $\sim$ 50 μm [88].

4.1.5 Neurobiology. Accurate delineation of brain tumor boundaries is a challenging task that is critical for improving the quality of resection while preserving normal tissue. Using XRI-CT, the authors of Ref. [58] observed multiple microvascular proliferations around peritumoral edema in the form of a tumor infiltration structure.

Alzheimer's disease is known to be associated with the presence of amyloid plaques in the affected brain. These plaques are very small, of the order of 5–200 microns, and have low natural contrast when using classical CT. Connor et al. [144] tested the effectiveness of using XRI-CT to measure plaques in a mouse brain model. Their experiment used excised brains from both wild-type and transgenic mice that had developed Alzheimer's disease plaques. The detected plaques were less than 30 μm in diameter, which can be improved in the future (the theoretical resolution limit is $\sim$ 2 μm). Therefore, XRI-CT should be able to

image even the smallest plaques with a diameter of 5 μm without employing a contrast agent. One challenge the authors foresee in the future is visualizing the brain inside the skull: CT artifacts may obscure the very low contrast resolution (2%) of plaques. One way to avoid this situation would be to image at much higher energies, where skull artifacts could be significantly reduced. The radiation dose required to obtain high resolution precludes the use of the *in vivo* method in humans, but would be a promising model for animal studies.

4.1.6 Other soft tissues. Breast tissue and lung tissue, naturally, are the soft tissues most widely studied using XRI and XRI-CT techniques. However, there are many other examples of soft tissues and small organs studied by these methods. Some examples, in addition to those already mentioned above, include studies of uterine leiomyoma [145], guinea pig cochlea [59], pigs' eyes [146], mouse viscera [147], stomachs with gastric cancer [148], and acupuncture points [149].

4.2 Materials science
Along with soft tissues, which are quasi-transparent to X-rays, XRI also visualizes absorbing elements of biomedical objects, such as bones. There are other examples of XRI studies of absorbing objects, for example, seeds [150] and nuts [151].

Recently, XRI has been successfully used in materials science [24]. The method can help speed up the development of new materials and solve many problems in understanding the significance of micro- and submicrostructures in materials science [152].

Specifically, the method was used to detect and quantify damage after cyclic loading in composites with an all-oxide ceramic matrix [41]. *In situ* experiments revealed the formation of cracks in fiber-reinforced plastics [153], showed the evolution of damage in metal matrix composites under tensile loads [154], quantified the porosity and pore orientation in cordierite ceramics for particulate filters [155], and observed the evolution of various types of porosity in the aluminum alloy AlSi10Mg during heat treatment [156]. The authors of Ref. [157] observed the development of microcracks in a $ZrO_2 - SiO_2$ composite when an external uniaxial stress was applied during the cooling branch of a thermal cycle. The determination of grain sizes and the density of microcracks in β-eucryptite ceramics obtained from glass was performed in Ref. [158]. XRI-CT made it possible to quantify the formation of microcracks under the influence of hydrogen in

duplex stainless steel [82]. In Ref. [40], the shape, size, nature, and distribution of discontinuities in the Inconel 718 alloy were assessed in samples subjected to hot isostatic pressing. In Refs [74, 81], XRI was used to detect the production of voids in parts made of Ti-6Al-4V alloy by selective laser melting. It was shown in Ref. [159] that cryogenic XRI can image structure II air hydrate and structure I carbon dioxide hydrate coexisting with ice and gas bubbles with a density resolution of about 0.01 g cm^{-3} and a wide range of dynamic densities of about 1.60 g cm^{-3}.

5. Conclusions

So, XRI demonstrates a significant improvement in contrast compared to standard radiographic visualization. Contrast is based not only on absorption, but also on the refractive and scattering properties of a sample. This visualization technique can improve image quality for medical applications, industrial radiography, and nondestructive testing.

Currently, various methods of phase-contrast radiography have been developed and used, along with XRI. When determining which visualization method to use for a particular problem, it is necessary to understand the technology of the systems and the relative advantages and disadvantages of each. In particular, XRI should be compared with the most commonly used methods: the propagation method and the Talbot interferometer. This is a complex task, as evidenced by the detailed and thorough analysis presented in Refs [160, 161]. From the conclusions presented in them, it follows that XRI has a number of advantages.

(1) There is no interaction of coherent X-ray beams, which is natural for interferometric methods (the propagation method and Talbot interferometer); this explains the low requirements imposed on the quality of the primary beam: for the experimental implementation of the XRI method, it is possible to use conventional laboratory equipment.

(2) XRI has the greatest sensitivity to phase shifts (the least is inherent in the propagation method) and can detect much smaller refraction angles than the Talbot interferometer.

(3) The sensitivity of the three methods under consideration depends differently on the X-ray energy. The signal-to-noise ratio is inversely proportional to the square of the energy ($\propto 1/E^2$) for the propagation method and the Talbot interferometer, while it is inversely proportional to the energy ($\propto 1/E$) for XRI. This means that XRI is especially preferred when use is made of high-energy X-rays. This circumstance contributes to a significant reduction in the radiation dose required for biomedical imaging *in vivo*.

(4) XRI is free from most artifacts characteristic of interferometric methods, in particular, from the phase wrapping artifact.

(5) Another advantage of XRI is that it is possible to obtain an enlarged image of the sample by using an asymmetric analyzer crystal [162]. This opens up new possibilities for observing the entire sample or areas of interest within a sample at optimal magnification.

The listed advantages give reason to hope that the XRI method will remain one of the most popular X-ray visualization methods, including in clinical practice.

The work was performed within the framework of the state assignment of the National Research Center, Kurchatov Institute.

References

1. Blokhin M A *Fizika Rentgenovskikh Luchei* (Physics of X-Rays) (Moscow: Gostekhizdat, 1957)
2. Bravin A, Fiedler S, Thomlinson W C *Proc. SPIE* **4682** 167 (2002)
3. Pisano E D et al. *Radiology* **214** 895 (2000)
4. Bonse U, Hart M *Appl. Phys. Lett.* **7** 99 (1965)
5. Momose A et al. *Jpn. J. Appl. Phys.* **42** L866 (2003)
6. Snigirev A et al. *Rev. Sci. Instrum.* **66** 5486 (1995)
7. Somenkov V A, Tkalich A K, Shil'shtein S Sh *Sov. Phys. Tech. Phys.* **36** 1309 (1991); *Zh. Tekh. Fiz.* **61** (22) 197 (1991)
8. Manushkin A A et al. *Med. Fiz.* (3) 34 (2005)
9. Podurets K M, Pogorelyi D K *Al'manakh Klinicheskoi Meditsiny* (17-1) 217 (2008)
10. Förster E, Goetz K, Zaumseil P *Kristall Tech.* **15** 937 (1980)
11. Ingal V N, Belyaevskaya E A *Tech. Phys.* **42** 59 (1997); *Zh. Tekh. Fiz.* **67** 68 (1997)
12. Davis T J et al. *Nature* **373** 595 (1995)
13. Gao D, Davis T J, Wilkins S W *Australian J. Phys.* **48** 103 (1995)
14. Ingal V N, Beliaevskaya E A *J. Phys. D* **28** 2314 (1995)
15. Ingal V N, Beliaevskaya E A *Nuovo Cimento D* **19** 553 (1997)
16. Ingal V N et al. *Phys. Med. Biol.* **43** 2555 (1998)
17. Bushuev V A, Ingal V N, Belyaevskaya E A *Cryst. Rep.* **41** 766 (1996); *Kristallografiya* **41** 808 (1996)
18. Bushuev V A, Ingal V N, Beliaevskaya E A *Cryst. Rep.* **43** 538 (1998); *Kristallografiya* **43** 538 (1998)
19. Chapman D et al. *Phys. Med. Biol.* **42** 2015 (1997)
20. Bushuev V A, Sergeev A A *Tech. Phys. Lett.* **24** 851 (1998); *Pis'ma Zh. Tekh. Fiz.* **24** (21) 55 (1998)
21. Bushuev V A, Beliaevskaya E A, Ingal V N *Nuovo Cimento D* **19** 513 (1997)
22. Suortti P, Keyriläinen J, Thomlinson W *J. Phys. D* **46** 494002 (2013)
23. Connor D M, Zhong Z *Curr. Radiol. Rep.* **2** (7) 55 (2014)
24. Mani D et al. *J. Imaging* **8** (8) 206 (2022)
25. Mollenhauer J et al. *Osteoarthr. Cartilage* **10** 163 (2002)
26. Parham C et al. *Academic Radiology* **16** 911 (2009)
27. Nesch I et al. *Rev. Sci. Instrum.* **80** 093702 (2009)
28. Muehleman C et al. *Academic Radiology* **16** 918 (2009)
29. Muehleman C et al. *Clinical Anatomy* **23** 530 (2010)
30. Keyriläinen J, Fernández M, Suortti P *Nucl. Instrum. Meth. Phys. Res. A* **488** 419 (2002)
31. Bravin A *J. Phys. D* **36** (10A) A24 (2003)
32. Petrakov A P *Tech. Phys.* **48** 607 (2003); *Zh. Tekh. Fiz.* **73** (5) 84 (2003)
33. Shul'pina I L, Ratnikov V V, Matveev O A *Phys. Solid State* **43** 579 (2001); *Fiz. Tverd. Tela* **43** 559 (2001)
34. Kikuta S, Kohra K *J. Phys. Soc. Jpn.* **29** 1322 (1970)
35. Kohra K, Ando M *Nucl. Instrum. Meth.* **177** 117 (1980)
36. Maksimenko A et al. *Meas. Sci. Technol.* **15** 1251 (2004)
37. Zhong Z et al. *Nucl. Instrum. Meth. Phys. Res. A* **450** 556 (2000)
38. Lider V V *J. Surf. Invest. X-Ray, Synch. Neutron Tech.* **3** 933 (2009); *Poverkhnost'. Rentgen., Sinkhrotron. Neitron. Issled.* (12) 40 (2009)
39. Martin T, Koch A *J. Synchrotron Rad.* **13** 180 (2006)
40. Laquai R et al. *Metall. Mater. Trans. A* **51** 4146 (2020)
41. Kupsch A et al. *Adv. Eng. Mater.* **24** 2100763 (2022)
42. Ando M et al. *Med. Phys.* **47** 5505 (2020)
43. Hönnicke M G et al. *Rev. Sci. Instrum.* **83** 113702 (2012)
44. Shulpina I L *J. Phys. D* **26** (4A) A82 (1993)
45. Peng H et al. *J. Appl. Cryst.* **54** 1225 (2021)
46. Hirano K et al. *Jpn. J. Appl. Phys.* **41** L595 (2002)
47. Ando M et al. *Jpn. J. Appl. Phys.* **41** L1016 (2002)
48. Kato N *Acta Cryst.* **14** 526 (1961)
49. Kato N *Acta Cryst.* **14** 627 (1961)
50. Ando M et al. *Jpn. J. Appl. Phys.* **40** L844 (2001)
51. Ando M et al. *Radiat. Phys. Chem.* **71** 899 (2004)
52. Ando M et al. *Eur. Radiol.* **24** 423 (2014)
53. Ando M et al. *Jpn. J. Appl. Phys.* **41** 4742 (2002)
54. Ando M et al. *Jpn. J. Appl. Phys.* **43** L1175 (2004)
55. Shimao D et al. *Nucl. Instrum. Meth. Phys. Res. A* **548** 129 (2005)
56. Ando M et al. *Jpn. J. Appl. Phys.* **44** L528 (2005)
57. Davis T J et al. *Phys. Rev. Lett.* **74** 3173 (1995)
58. Seo S-J et al. *Phys. Med. Biol.* **57** 1251 (2012)
59. Gao X et al. *Comput. Med. Imaging Graph.* **30** 339 (2006)

60. Paganin D et al. *Opt. Commun.* **234** 87 (2004)
61. Chapman D et al. *Rev. Sci. Instrum.* **67** 3360 (1996)
62. Sunaguchi N et al. *Appl. Phys. Lett.* **97** 153701 (2010)
63. Ando M et al. *Phys. Med. Eur. J. Med. Phys.* **32** 1801 (2016)
64. Ando M et al. *Phys. Med. Eur. J. Med. Phys.* **79** 188 (2020)
65. Maksimenko A *Appl. Phys. Lett.* **90** 154106 (2007)
66. Chen Z-Q et al. *Chinese Phys. C* **33** 969 (2009)
67. Hu C et al. *Opt. Express* **16** 16704 (2008)
68. Hall M M (Jnr.) et al. *J. Appl. Cryst.* **10** 66 (1977)
69. Kitchen M J et al. *Phys. Med. Biol.* **52** 4171 (2007)
70. Kitchen M J et al. *Opt. Express* **18** 19994 (2010)
71. Kitchen M J et al. *Phys. Med. Biol.* **56** 515 (2011)
72. Rigon L et al. *J. Phys. D* **36** A107 (2003)
73. Rigon L, Arfelli F, Menk R-H *J. Phys. D* **40** 3077 (2007)
74. Laquai R et al. *Mater. Res. Lett.* **6** 130 (2018)
75. Arfelli F, Rigon L, Menk R H *Phys. Med. Biol.* **55** 1643 (2010)
76. Izadifar Z et al. *BioMed. Eng. OnLine* **14** 91 (2015)
77. Jud C et al. *Sci. Rep.* **11** 14017 (2021)
78. Arfelli F et al. *Sci. Rep.* **8** 362 (2018)
79. Fernández M et al. *Phys. Med. Biol.* **50** 2991 (2005)
80. Rigon L et al., in *X-TOP. 2002 Biennal Conf. on High-Resolution X-Ray Diffraction and Imaging, Grenoble*
81. Laquai R et al. *Matls. Perf. Charact.* **9** 82 (2020)
82. Laquai R et al. *Adv. Eng. Mater.* **24** 2101287 (2022)
83. Diemoz P C et al. *Opt. Express* **18** 3494 (2010)
84. Rigon L, Arfelli F, Menk R *Appl. Phys. Lett.* **90** 114102 (2007)
85. Pagot E et al. *Appl. Phys. Lett.* **82** 3421 (2003)
86. Oltulu O et al. *J. Phys. D* **36** 2152 (2003)
87. Wernick M N et al. *Phys. Med. Biol.* **48** 3875 (2003)
88. Hu C et al. *Prog. Nat. Sci.* **19** 955 (2009)
89. Brankov J G et al. *Med. Phys.* **33** 278 (2006)
90. Huang Z, Kang K, Yang Y *Nucl. Instrum. Meth. Phys. Res. A* **579** 218 (2007)
91. Huang Z-F et al. *Phys. Med. Biol.* **52** 1 (2007)
92. Nesterets Ya I et al. *Acta Cryst. A* **62** 296 (2006)
93. Suhonen H et al. *J. Synchrotron Rad.* **14** 512 (2007)
94. Fernández M et al. *Eur. J. Radiol.* **68** S89 (2008)
95. Dilmanian F A et al. *Phys. Med. Biol.* **45** 933 (2000)
96. Maksimenko A et al. *Appl. Phys. Lett.* **86** 124105 (2005)
97. Khelashvili G et al. *Phys. Med. Biol.* **51** 221 (2006)
98. Pavlov K M et al. *J. Phys. D* **34** A168 (2001)
99. Liu Y J et al. *Phys. Med. Biol.* **52** L5 (2007)
100. Wang Z-T et al. *Chinese Phys. C* **33** 975 (2009)
101. Gilbert P *J. Theor. Biol.* **36** 105 (1972)
102. Majidi K et al. *Phys. Med. Biol.* **59** 3483 (2014)
103. Sunaguchi N, Yuasa T, Ando M *Appl. Phys. Lett.* **103** 143702 (2013)
104. Sunaguchi N et al. *PLoS One* **10** e0135654 (2015)
105. Dobbins J T (III), Godfrey D J *Phys. Med. Biol.* **48** R65 (2003)
106. Shimao D et al. *Jpn. J. Appl. Phys.* **46** L608 (2007)
107. Shimao D et al. *Eur. J. Radiol.* **68** S27 (2008)
108. Sunaguchi N et al. *Appl. Phys. Lett.* **99** 103704 (2011)
109. Sunaguchi N et al. *J. Phys. Conf. Ser.* **425** 192012 (2013)
110. Helfen L et al. *Appl. Phys. Lett.* **86** 071915 (2005)
111. Helfen L et al. *Rev. Sci. Instrum.* **82** 063702 (2011)
112. Hirano K et al. *J. Synchrotron Rad.* **23** 1484 (2016)
113. Fiedler S et al. *Phys. Med. Biol.* **49** 175 (2004)
114. Bravin A et al. *Phys. Med. Biol.* **52** 2197 (2007)
115. Keyriläinen J et al. *Radiology* **249** 321 (2008)
116. Kao T et al. *Phys. Med. Biol.* **54** 3247 (2009)
117. Keyriläinen J et al. *Acta Radiol.* **51** 866 (2010)
118. Keyriläinen J et al. *J. Synchrotron Rad.* **18** 689 (2011)
119. Zhao Y et al. *Proc. Natl. Acad. Sci. USA* **109** 18290 (2012)
120. Faulconer L S et al. *Academic Radiology* **17** 433 (2010)
121. Kiss M Z et al. *Phys. Med. Biol.* **49** 3427 (2004)
122. Li J et al. *J. Anatomy* **202** 463 (2003)
123. Li J et al. *Osteoarthr. Cartilage* **13** 187 (2005)
124. Li J et al. *Osteoarthr. Cartilage* **17** 1193 (2009)
125. Muehleman C et al. *J. Am. Podiatric Med. Assoc.* **94** 453 (2004)
126. Muehleman C et al. *J. Am. Podiatric Med. Assoc.* **99** 95 (2009)
127. Muehleman C et al. *J. Anatomy* **208** 115 (2006)
128. Majumdar S et al. *Eur. Radiol.* **14** 1440 (2004)
129. Muehleman C et al. *Osteoarthr. Cartilage* **12** 97 (2004)
130. Cooper D M L et al. *Can. Assoc. Radiol. J.* **62** 251 (2011)
131. Li J et al. *Foot Ankle Int.* **27** 344 (2006)
132. Shimao D et al. *Appl. Radiat. Isotop.* **64** 868 (2006)
133. Coan P et al. *Eur. J. Radiol.* **68** S41 (2008)
134. Wagner A et al. *Phys. Med. Biol.* **51** 1313 (2006)
135. Connor D M et al. *Phys. Med. Biol.* **51** 3283 (2006)
136. Izadifar Z, Chapman L D, Chen X *Tissue Eng. C* **20** 140 (2014)
137. Kitchen M J et al. *Br. J. Radiol.* **78** 1018 (2005)
138. Kitchen M J et al. *Eur. J. Radiol.* **68** S49 (2008)
139. Kitchen M J et al. *Biomed. Opt. Express* **11** 4176 (2020)
140. Connor D M et al. *Academic Radiology* **18** 1515 (2011)
141. Zhang X et al. *Eur. Radiol.* **23** 417 (2013)
142. Duan J et al. *PLoS ONE* **8** (10) e78176 (2013)
143. Hu D et al. *PLoS ONE* **9** (2) e87957 (2014)
144. Connor D M et al. *NeuroImage* **46** 908 (2009)
145. Liu C et al. *Med. Sci. Monit.* **11** 33 (2005)
146. Kelly M E et al. *Can. J. Ophthalmol.* **42** 731 (2007)
147. Zhang X et al. *Am. J. Roentgenol.* **195** 545 (2010)
148. Tang L et al. *J. Synchrotron Rad.* **19** 319 (2012)
149. Yan X H et al. *J. Phys. Conf. Ser.* **186** 012100 (2009)
150. Young L W et al. *J. Exp. Botany* **58** 2513 (2007)
151. Rao D V et al. *Food Measure.* **7** 13 (2013)
152. Müller B R et al. *Mater. Test.* **46** 314 (2004)
153. Kupsch A et al. *IOP Conf. Ser. Mater. Sci. Eng.* **942** 012035 (2020)
154. Nellesen J et al. *J. Mater. Sci.* **53** 6021 (2018)
155. Kupsch A et al. *J. Ceram. Sci. Tech.* **4** 169 (2013)
156. Serrano-Munoz I et al. *Mater. Sci. Eng. A* **838** 142732 (2022)
157. Laquai R et al. *Materials* **12** 1017 (2019)
158. Müller B R et al. *Acta Mater.* **144** 627 (2018)
159. Takeya S et al. *J. Synchrotron Rad.* **19** 1038 (2012)
160. Diemoz P C, Bravin A, Coan P *Opt. Express* **20** 2789 (2012)
161. Diemoz P C et al. *Opt. Express* **20** 27670 (2012)
162. Hirano K et al. *J. Synchrotron Rad.* **29** 787 (2022)